Azo compounds as a family of organic electrode materials for alkali-ion batteries

Chao Luo[a], Oleg Borodin[b], Xiao Ji[a,c], Singyuk Hou[a], Karen J. Gaskell[d], Xiulin Fan[a], Ji Chen[a], Tao Deng[a], Ruixing Wang[d], Jianjun Jiang[c], and Chunsheng Wang[a,1]

[a]Department of Chemical and Biomolecular Engineering, University of Maryland, College Park, MD 20742; [b]Electrochemistry Branch, Sensors and Electron Devices Directorate, US Army Research Laboratory, Adelphi, MD 20783; [c]School of Optical and Electronic Information, Huazhong University of Science and Technology, 430074 Wuhan, Hubei, China; and [d]Department of Chemistry and Biochemistry, University of Maryland, College Park, MD 20742

Edited by Thomas E. Mallouk, The Pennsylvania State University, University Park, PA, and approved January 17, 2018 (received for review October 12, 2017)

Organic compounds are desirable for sustainable Li-ion batteries (LIBs), but the poor cycle stability and low power density limit their large-scale application. Here we report a family of organic compounds containing azo group (N=N) for reversible lithiation/delithiation. Azobenzene-4,4′-dicarboxylic acid lithium salt (ADALS) with an azo group in the center of the conjugated structure is used as a model azo compound to investigate the electrochemical behaviors and reaction mechanism of azo compounds. In LIBs, ADALS can provide a capacity of 190 mAh g^{-1} at 0.5 C (corresponding to current density of 95 mA g^{-1}) and still retain 90%, 71%, and 56% of the capacity when the current density is increased to 2 C, 10 C, and 20 C, respectively. Moreover, ADALS retains 89% of initial capacity after 5,000 cycles at 20 C with a slow capacity decay rate of 0.0023% per cycle, representing one of the best performances in all organic compounds. Superior electrochemical behavior of ADALS is also observed in Na-ion batteries, demonstrating that azo compounds are universal electrode materials for alkali-ion batteries. The highly reversible redox chemistry of azo compounds to alkali ions was confirmed by density-functional theory (DFT) calculations. It provides opportunities for developing sustainable batteries.

azo compounds | alkali-ion batteries | organic electrode materials | sustainable batteries | high power density

Li-ion batteries (LIBs) are the main energy storage devices for most portable electronics and electric vehicles. However, the widespread application of LIBs induces environmental challenges such as greenhouse effect and heavy metal pollution (1, 2), stimulating the development of green and sustainable materials as substitutions for the commercially used inorganic $LiCoO_2$ and graphite electrode materials. Organic materials with the advantages of light weight, abundance, low cost, sustainability, and recyclability are desirable for green and sustainable LIBs (3–5). Therefore, designing and synthesizing high-performance organic electrode materials are pivotal for the development of LIBs.

In the last three decades, four types of organic materials, organosulfur compounds, organic free-radical compounds, carbonyl (C=O) compounds, and imine (C=N) compounds, have been explored for high-performance LIB electrodes (6–16). Extensive research has been conducted to enhance the electrochemical performance of these organic electrodes, but only limited advance has been achieved due to some intrinsic issues of these organic compounds. In these four types of organic materials, because the organosulfur compounds suffer from sluggish reaction kinetics and organic free-radical compounds have low energy density, the current investigation is mainly focused on carbonyl compounds and imine compounds, which contain two or more carbonyl or imine groups in the conjugated structure. Although a few carboxylates (terephthalate, heteroaromatic carbonyl compounds) and polymers (polyanthraquinone and polyimides) exhibit promising battery performance (17–22), the terephthalate cannot maintain its capacity at a high current density due to its poor conductivity, while the heteroaromatic carbonyl compounds and polymers face challenges of complicated and time-/energy-consuming synthetic procedure. Imine compounds (modified pteridine compounds and π-conjugated *N*-containing heteroaromatic compounds) display high electrochemical performance in LIBs (13, 14), but a large amount (>50 wt %) of carbon is needed in the organic electrodes due to the low electronic conductivity, which lowers the energy density of organic electrodes (23). Hence, it is vital to explore new organic compounds with a simple synthetic route, high cycling stability, and fast charge/discharge capability.

Herein, we report a type of organic compounds which contain azo (N=N) active groups, for superior LIBs. Unlike carbonyl compounds and imine compounds, which require two or more functional groups connected by a conjugated structure in one molecular unit to maintain the electrochemical activity, the azo compounds only contain one azo functional group, and the azo group can reversibly react with two Li ions (Fig. 1), which simplifies the structure design and modification. In this work, three azo compounds, azobenzene (AB), methyl red sodium salt, (MRSS) and azobenzene-4,4′-dicarboxylic acid lithium salt (ADALS) that contain π-conjugated structure with an azo group in the center (Fig. 1 *A*–*C*) are employed as model materials to study the lithiation/delithiation mechanism and electrochemical performance in LIBs. Among these three azo compounds, AB has a simple π-conjugated structure with an azo group in the center, so it is used as a basic compound to study the lithiation/delithiation on

Significance

Organic electrode materials are promising for green and sustainable secondary batteries due to the light weight, abundance, low cost, sustainability, and recyclability of organic materials. However, the traditional organic electrodes suffer from poor cycle stability and low power density. Here, we report a family of organic electrode materials containing azo functional groups for alkali-ion batteries. The azo compound, azobenzene-4,4′-dicarboxylic acid lithium salt, exhibits superior electrochemical performance in Li-ion and Na-ion batteries, in terms of long cycle life and high rate capability. The mechanism study demonstrates that the azo group can reversibly react with Li ions during charge/discharge cycles. Therefore, this work offers opportunities for developing stable and high-rate alkali-ion batteries.

Author contributions: C.L. and C.W. designed research; C.L., O.B., X.J., S.H., K.J.G., X.F., J.C., and R.W. performed research; C.L. contributed new reagents/analytic tools; C.L., O.B., T.D., J.J., and C.W. analyzed data; and C.L. and C.W. wrote the paper.

The authors declare no conflict of interest.

This article is a PNAS Direct Submission.

[1]To whom correspondence should be addressed. Email: cswang@umd.edu.

This article contains supporting information online at www.pnas.org/lookup/suppl/doi:10.1073/pnas.1717892115/-/DCSupplemental.

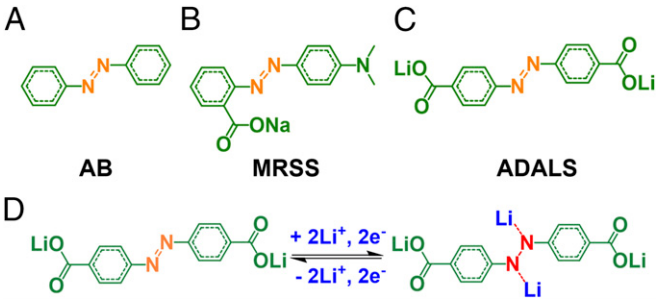

Fig. 1. Molecular structure of (*A*) AB, (*B*) MRSS, and (*C*) ADALS. (*D*) Reaction mechanism for ADALS.

an active azo group (N=N). As evidenced by the dissolution test in *SI Appendix*, Fig. S1, AB is soluble in the commercial carbonate-based electrolyte to form an orange solution. These solubility trends are consistent with dissolution free energies of the representative clusters in AB, Li_2(AB), and ADALS estimated from DFT calculations. As shown in *SI Appendix*, Fig. S2, the free energy of the cluster dissolution follows the order (AB) < (Li_2AB) < (ADALS), indicating that the nonlithiated (AB) crystal is the most prone to dissolution followed by the lithiated AB crystal. High free-energy penalty for dissolving the ADALS cluster is due to high cohesive energy density arising from the strong Li···O bonds that are present in ADALS crystal. Alternatively, AB is considered soluble in the organic electrolyte, because its polarity is very close to the polarity of the carbonate-based electrolyte. It has been reported that adding Li–O or COO–Li groups into the organic electrode materials can effectively enhance the polarity of organic materials, thus decreasing the solubility in the electrolyte (10, 17). The solubility of azo compounds in carbonate-based electrolyte can be reduced by enhancing their polarities through salt formation. Herein, the carboxylate groups are added to AB to suppress the solubility in the carbonate-based electrolyte. Therefore, an extra carboxylate group is added at the *ortho*- position in MRSS. However, it is still soluble in the electrolyte as evidenced by the orange solution in *SI Appendix*, Fig. S3. To suppress the dissolution of azo compounds, two extra carboxylate groups are added at the *para*- position in ADALS to decrease the solubility in the electrolyte. An ADALS electrode with 30 wt% conductive carbon exhibits one of the best electrochemical performance among organic electrode materials. It retains a reversible capacity of 179 mAh g^{-1} at 0.5 C for 100 cycles (1 C = 190 mA g^{-1}), and a reversible capacity of 146 mAh g^{-1} at 2 C for 2,000 cycles. Moreover, ADALS can deliver a reversible capacity of 105 mAh g^{-1} even at a high current density of 20 C, and a capacity of 93 mAh g^{-1} is retained after 5,000 cycles. The fast charge/discharge capability of ADALS is ascribed to the extended π-conjugated structure in the aromatic azo compound and strong adsorption toward Li^+ by nitrogen in the azo group (24). The detailed characterizations using X-ray diffraction (XRD), Raman spectroscopy, X-ray photoelectron spectroscopy (XPS), and DFT calculations confirm the reversible reaction between the azo group and Li ion in LIBs. In addition, ADALS delivers a reversible capacity of 160 mAh g^{-1} at 1 C in Na-ion batteries (SIBs) and retains 92% of its initial capacity after 500 cycles, demonstrating the excellent electrochemical behavior in SIBs. Therefore, azo compounds with exceptional electrochemical performance are universal for alkali-ion batteries.

Results and Discussion

Materials Characterization. The structure and physical properties of three azo model compounds (AB, MRSS, and ADALS) were characterized using XRD, Raman spectroscopy, FTIR, thermal gravimetric (TG) analysis, and scanning electron microscopy (SEM). As demonstrated by XRD patterns in *SI Appendix*, Figs. S4*A*, S5*A*, and S6*A*, all three azo compounds show crystal structures. The peaks at 1,400–1,450 cm^{-1} range in Raman spectra (*SI Appendix*, Figs. S4*B*, S5*B*, and S6*B*) and peaks at 1,575–1,630 cm^{-1} range in FTIR spectra (*SI Appendix*, Figs. S4*C*, S5*C*, and S6*C*) confirm the existence of an azo group in these three compounds (25, 26). The good match between the calculated spectrum for $(AB)_3$ and experiments shown in *SI Appendix*, Fig. S7 further confirms that the examined compound is indeed AB. Moreover, the elevated baseline intensity with the increase of wavenumber in Raman spectra (*SI Appendix*, Figs. S4*B*, S5*B*, and S6*B*) is due to the fluorescence emitted by azo compounds. TG analysis (*SI Appendix*, Figs. S4*D*, S5*D*, and S6*D*) displays that AB begins to lose weight at 100 °C due to its low melting and boiling point, while MRSS and ADALS are stable up to 275 °C and 410 °C, respectively. The morphology of MRSS and ADALS in the SEM images (*SI Appendix*, Figs. S5*E* and S6*E*) indicates that MRSS and ADALS consist of large particles with a size of about 2 μm.

Electrochemical Property. The electrochemical performance of AB, MRSS, and ADALS was measured using coin cells in high-concentration electrolyte [6 M Lithium bis(trifluoromethanesulfonyl)imide (LiTFSI) in 1,3-dioxolane/dimethoxyethane (DOL/DME)] to suppress the dissolution of AB and MRSS in the electrolyte. All cells were cycled at 0.5 C in the cutoff window between 1.0 and 3.0 V. As shown in *SI Appendix*, Fig. S8*A*, AB exhibits two pairs of long and sloping discharge/charge plateaus at 1.9/2.5 V and 1.55/1.8 V, respectively. Since the azo group is the only active site for lithiation/delithiation in AB (Fig. 1*A*), the capacity of AB in *SI Appendix*, Fig. S8 is attributed to the reaction between the azo group and Li ions, proving that azo compounds with an N=N bond can function as a type of organic electrodes for LIBs. However, due to the high solubility in the electrolyte, AB exhibits poor cycling stability (*SI Appendix*, Fig. S8*B*). To reduce the solubility, a carboxylate group is added at the *ortho*- position in MRSS. In *SI Appendix*, Fig. S8*C*, MRSS exhibits a pair of long and flat charge/discharge plateaus centered at 1.6 V with a reversible capacity of ∼110 mAh g^{-1}. In the long-term cycling test (*SI Appendix*, Fig. S8*D*), the capacity increases in the initial five cycles, and then decreases from the 5th to the 30th cycle due to the dissolution of MRSS in the electrolyte. Therefore, adding a carboxylate group at the *ortho*- position of AB cannot suppress the dissolution of MRSS. The high Coulombic efficiency of ∼120% induced by the shuttle reaction also provides evidence for the dissolution of MRSS in electrolyte during lithiation/delithiation. Although adding carboxylate group at the *ortho*- position does not overcome the dissolution issue, it does change the lithiation/delithiation potentials.

To reduce the dissolution of AB in the electrolyte, two carboxylate groups are introduced in the aromatic azo compound to generate ADALS, which shows high cycling stability in LIBs. In Fig. 2*A*, ADALS shows two pairs of long and flat charge/discharge plateaus at 1.5 and 1.55 V, respectively, with a reversible capacity of 190 mAh g^{-1}, which is close to the theoretical capacity (190.1 mAh g^{-1}) of ADALS. The cyclic voltammetry (CV) of ADALS in Fig. 2*B* shows one wide cathodic peak at 1.45 V from the overlap of two cathodic peaks, and two anodic peaks at 1.55 and 1.65 V, corresponding to the two pairs of charge/discharge plateaus in Fig. 2*A*. In the long-term cycling test (Fig. 2*C*), a reversible capacity of 175 mAh g^{-1} is retained after 100 cycles with a slow capacity decay rate of 0.078% per cycle, and the Coulombic efficiency is close to 100%, demonstrating superior cycling stability of ADALS. The rate capability of ADALS is evaluated at various current densities from 0.5 to 20 C. In Fig. 2*D*, ADALS delivers a reversible capacity of 190 mAh g^{-1} at 0.5 C, and retains a capacity of 105 mAh g^{-1} even at a high current density of 20 C. The mechanism for fast charge and discharge behaviors and long cycling stability of ADALS were

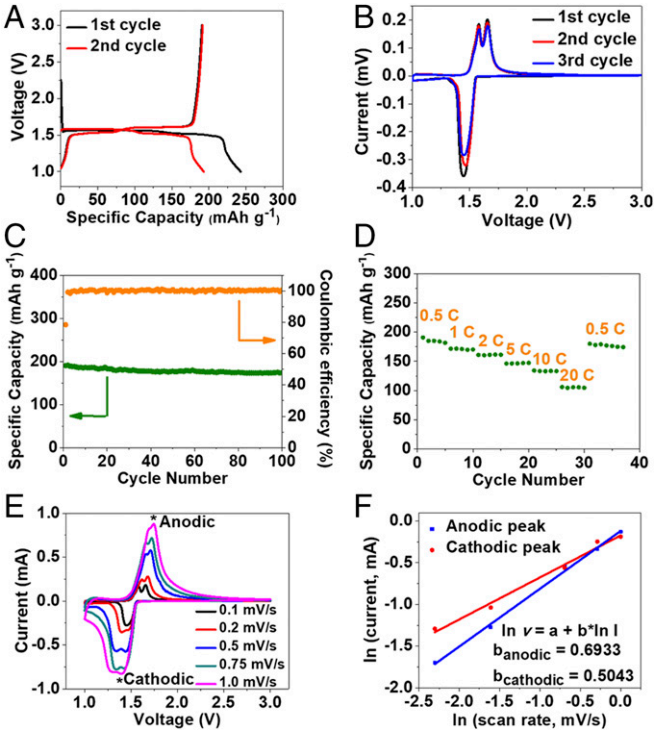

Fig. 2. The electrochemical performance of ADALS in LIBs with 6 M LiTFSI in DOL/DME electrolyte. (*A*) The galvanostatic charge–discharge curves. (*B*) Cyclic voltammograms at 0.1 mV s^{-1}. (*C*) Delithiation capacity and Coulombic efficiency versus cycle number at the current density of 0.5 C. (*D*) Rate performance at various C rates; (*E*) CV curves of ADALS at various scan rates. (*F*) The ln relationship of peak current and scan rate for ADALS.

investigated using electrochemical impedance spectroscopy (EIS). *SI Appendix*, Fig. S9 shows the EIS evolution of ADALS electrode at different charge/discharge cycles. The interface resistance of ADALS electrode, represented by the depressed semicircle, increases from ~30 to ~50 Ω after five cycles and then stabilizes at ~50 Ω during subsequent cycles. The low interface resistance of ADALS after cycling enables fast charge–discharge capability. In addition to interface reaction kinetics, the Li-ion diffusion kinetics was also investigated using CV. Fig. 2*E* shows the CV curves of ADALS at different scan rates. With elevated scan rate, the cathodic peaks shift to lower potential, while the anodic peaks shift to higher potential, ascribing to the enhanced polarization. The linear fit of natural logarithm ln relationship of peak current and scan rate in Fig. 2*F* shows that the slopes of both anodic and cathodic peaks are close to 0.5, demonstrating the lithiation/delithiation kinetics of ADALS is determined by Li-ion diffusion (27). Since ADALS consists of microsized particles, minimizing the particle size can further enhance the rate capability. As reported by Lei and coworkers (28), extending the π-conjugated system of terephthalate salt increases the high rate performance of carbonyl compound in SIBs. Moreover, the nitrogen-containing electron donor group has strong interaction with Li ion (24). Therefore, the high rate capability of an azo-based electrode is attributed to the extended π-conjugated system in ADALS and strong Li^+ adsorption by nitrogen in the azo group.

The high cycling stability of ADALS in 6 M LiTFSI-DOL/DME electrolyte (Fig. 2*C*) demonstrates that adding two carboxylate groups in the aromatic azo compound can effectively suppress the dissolution of ADALS in high-concentration electrolyte during charge/discharge. The electrochemical behaviors of ADALS in dilute commercial electrolyte [1 M $LiPF_6$ in EC/diethyl carbonate (DEC)] were also investigated using coin cells for practical application. As shown in Fig. 3*A*, the galvanostatic charge–discharge curves of ADALS in commercial electrolyte are similar to that in high-concentration electrolyte (Fig. 2*A*), and a reversible capacity of 190 mAh g^{-1} is retained in the commercial electrolyte. The first-cycle Coulombic efficiency (FCE) of ADALS in LIBs is 77%. The low FCE is due to the formation of a solid electrolyte interface (SEI) layer on carbon black in an ADALS electrode. As shown in *SI Appendix*, Fig. S10*A*, the first-cycle charge/discharge capacities of carbon black are 50.6 and 28.3 mAh g^{-1}, respectively, with a low FCE of 56%. Since the ADALS electrode contains 30 wt % carbon black, the low FCE of carbon black decreases the FCE of an ADALS electrode. To improve the FCE, the content of carbon black in an ADALS electrode is decreased from 30 to 15 wt %. The FCE of an ADALS electrode with 15 wt % carbon black is increased to 86.2% as shown in *SI Appendix*, Fig. S10*B*. The other method to improve the FCE is using more stable ether-based electrolyte (1 M LiTFSI-DOL/DME electrolyte) to suppress the formation of the SEI layer (29). As shown in *SI Appendix*, Fig. S10*C*, the FCE of an ADALS electrode is improved to 82.5% in the ether-based electrolyte. Therefore, decreasing carbon black content and using ether-based electrolyte are two effective methods to enhance the FCE of an ADALS electrode in LIBs. In the long-term cycling test (Fig. 3*B*), a reversible capacity of 179 mAh g^{-1} at 0.5 C is retained after 100 cycles. When the current density enhances to 2 C, similar charge–discharge curves are observed in Fig. 3*C*, and a reversible capacity of 146 mAh g^{-1} is retained for 2,000 cycles (Fig. 3*D*), demonstrating its exceptional cycling

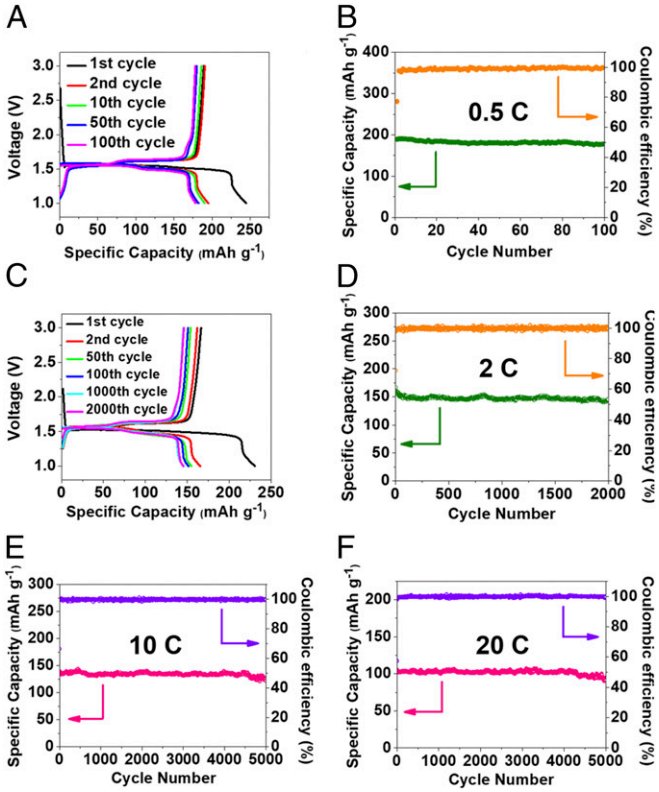

Fig. 3. The electrochemical performance of ADALS in LIBs with 1 M $LiPF_6$ in EC/DEC electrolyte. (*A*) The galvanostatic charge–discharge curves at 0.5 C. (*B*) Delithiation capacity and Coulombic efficiency versus cycle number at the current density of 0.5 C. (*C*) The galvanostatic charge–discharge curves at 2 C. Delithiation capacity and Coulombic efficiency versus cycle number at 2 C (*D*), 10 C (*E*), and 20 C (*F*).

stability. When the current density is further increased to 10 and 20 C, the reversible capacity of ADALS is retained at 126 and 93 mAh g^{-1}, respectively, after 5,000 cycles (Fig. 3 *E* and *F*) with a very slow capacity decay rate of 0.0023% per cycle, suggesting the robust reaction kinetics and superior cycling stability. More importantly, the Coulombic efficiency of ADALS in the commercial electrolyte is close to 100% at various current density, indicating the dissolution of the azo compound is effectively mitigated by adding two carboxylate groups in the azo compound. The excellent electrochemical performance of ADALS in commercial electrolyte demonstrates the high potential for commercialization of an azo compound for the next generation of green LIBs.

Reaction Mechanism. XRD, Raman spectroscopy, XPS, and DFT calculations were conducted to understand the reaction mechanism behind the excellent battery performance of ADALS. As shown in XRD patterns (Fig. 4*A*), after lithiation, the XRD peaks of a pristine ADALS electrode at 20.2°, 22.0°, and 23.2° disappear, while a broad peak at 20.7° appears, demonstrating the phase change occurs during lithiation. This XRD peak stands for the formation of a phase at fully discharged state. After being fully charged to 3 V, the ADALS electrode retains its original crystal structure, demonstrating good reversibility of ADALS in LIBs. However, compared with the XRD peaks of a pristine ADALS, the peak width becomes broader and the signal strength becomes weaker after five cycles, demonstrating the crystallinity of ADALS particles decreases after charge/discharge cycles. The reduced crystallinity of cycles is attributed to pulverization of the ADALS particle and the large strain/stress induced by large volume changes in lithiation/delithiation cycles. The reduction of crystallinity after charge/discharge cycles was also reported in high-capacity Si and Sn electrodes (30, 31). In the Raman spectra (Fig. 4*B*), when ADALS is fully discharged to 1.0 V, the characteristic Raman peak at 1,450 cm^{-1} for azo group in the pristine ADALS electrode disappears. Instead, a peak at 1,370 cm^{-1}, representing the lithiated azo group (Li-*N*-*N*-Li), appears at 1 V, demonstrating the azo group reacts with Li ion during the lithiation process. When an ADALS electrode is charged back to 3 V, the characteristic Raman peak at 1,450 cm^{-1} for an azo group recovers, demonstrating reversible electrochemical reaction between the azo group and Li ion. In addition, the Raman peak at 1,600 cm^{-1} for the carbonyl group in ADALS does not change upon cycling, indicating the carbonyl group does not participate in the reaction with Li ion. Raman spectra also show that the peaks between 1,100 and 1,200 cm^{-1} largely disappear upon ADALS discharge to 1 V and a peak around 1,000 cm^{-1} appears. DFT calculations using two different density functionals of the fully lithiated (discharged) ADALS (Li_4ADA) and fully delithiated (charged) ADALS (Li_2ADA) shown in *SI Appendix*, Figs. S11 and S12 reproduce these trends, with the peak slightly below 1,200 cm^{-1} largely disappearing while the peaks slightly below 1,000 cm^{-1} appearing upon lithiation of the azo group in accord with experimental observation. DFT calculations of the partially lithiated ADALS (Li_3ADA) shown in *SI Appendix*, Fig. S12 indicate a small peak around 1,100–1,200 cm^{-1}, indicating that a small Raman peak of ADALS at 1 V shown in Fig. 4*A* is likely due to a small presence of the partially lithiated material. In summary, DFT calculations of the Raman spectra of Li_2ADA, Li_3ADA, and Li_4ADA confirm Li···*N*-*N*···Li bond formation during cycling of ADALS.

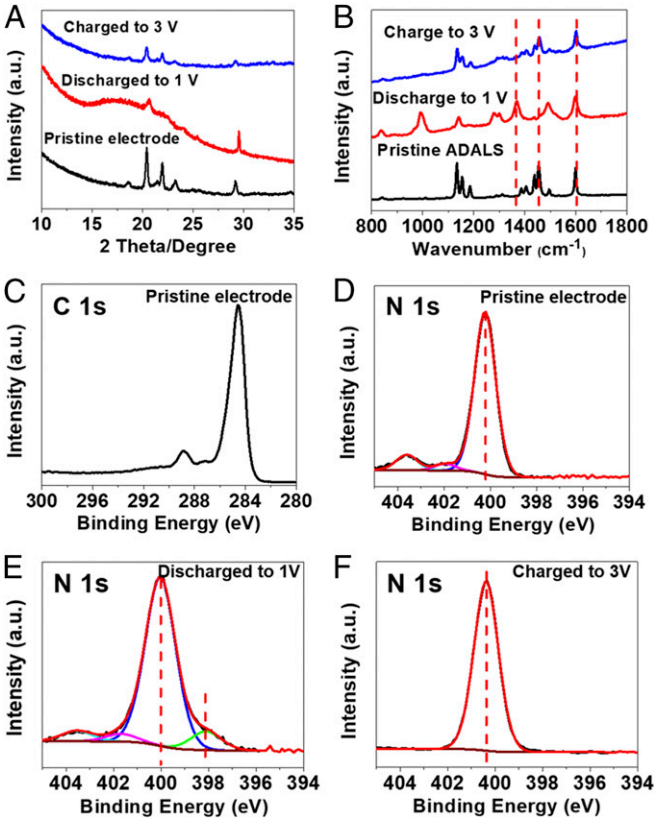

Fig. 4. (*A*) XRD spectra of ADALS electrodes before and after five cycles. (*B*) Raman spectra of ADALS electrodes before and after five cycles. XPS spectra of ADALS electrodes before (*C*) C 1 s, (*D*) N 1 s and after two cycles at 1 V for N 1 s (*E*) and at 3 V for N 1 s (*F*).

The reversible electrochemical reaction at an N=N bond is further confirmed by XPS in Fig. 4 *C*–*F*, where the C 1s peak at 284.6 eV in pristine ADALS (Fig. 4*C*) is used as a reference binding energy. The XPS of a pristine ADALS electrode (Fig. 4*D*) shows a strong and sharp characteristic XPS peak at 400.2 eV for the azo group in the pristine ADALS (32). The two small peaks at 401.8 and 403.6 eV stand for the oxidized nitrogen, coming from the impurity of ADALS. As shown in *SI Appendix*, Fig. S13, the C 1s peak at 284.6 eV is also used as a reference binding energy at the fully discharged state. When an ADALS electrode is discharged to 1 V, a peak at 398.3 eV, representing a lithiated azo group, appears (Fig. 4*E*). This peak position is similar to the XPS peak for the lithiated imine group in the literature (13). However, the azo peak at 400.2 eV is still strong at the fully discharged state, probably because of the existence of organic nitrogen matrix in the SEI layer. The organic nitrogen matrix could be amide [*N*-(C=O)-O], imide [(C= O)-*N*-(C=O)], or polyaniline [$(C_6H_4NH)_x$], which exhibit N 1s XPS peak at ~400.4 eV (33–36). It is possible that the azo compound is reduced during lithiation, and reacts with carbonate-based electrolyte to generate amide, imide, or polyaniline as the SEI layer on the surface of ADALS electrode. As indicated by the survey of pristine and cycled ADALS electrodes, the fluorine peak, which does not exist in the pristine electrode (*SI Appendix*, Fig. S14*A*), grows up in the cycled electrode (*SI Appendix*, Fig. S14 *B* and *C*). It comes from a main inorganic component (LiF) in the SEI and some residual $LiPF_6$. Quantum chemistry (QC) calculations of the reduction potentials of the $LiPF_6$-EC/DEC electrolyte components shown in *SI Appendix*, Fig. S15 predict that reduction of the $(LiPF_6)_2$ salt and (Li_2DEC) aggregates is expected to occur within the operating range of ADALS cathodes with reduction potentials of 1.6 and 1.3 V vs. Li/Li^+, respectively. Reduction of $(LiPF_6)_2$ salt yields LiF in accord with the experimental XPS observation of LiF in the SEI. QC calculations predict that reduction of the Li^+(EC) and Li^+(DEC) solvates where the solvent is coordinated by only one Li^+ occurs at much lower potentials <0.61 V vs. Li/Li^+. Since XPS only

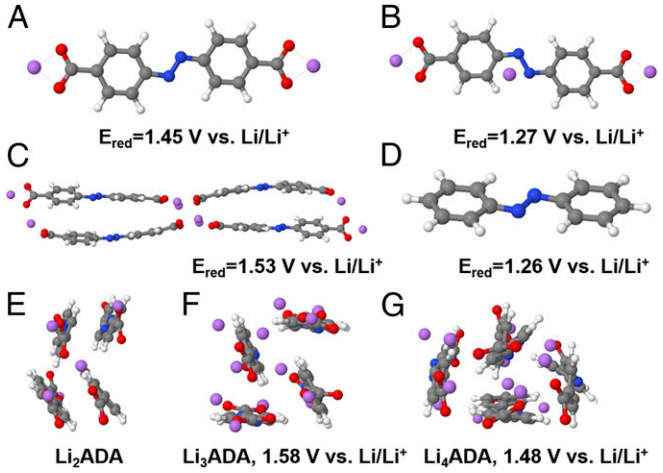

Fig. 5. Reduction potentials from M05-2X/6–31 + G(d,p) DFT calculations of Li_2-ADA (*A*), Li_3-ADA (*B*), $(Li_2\text{-ADA})_4$ (*C*), and AB (*D*) complexes immersed in implicit solvent modeled using SMD(ether) solvation model. The optimized crystal structures of Li_2ADA, Li_3ADA, and Li_4ADA from periodic DFT calculations containing four ADA molecules per simulation cell (*E*–*G*) using Perdew–Burke–Ernzerhof (PBE) functional. Intercalation potentials of Li_3-ADA and Li_4ADA vs. Li/Li^+ are also given.

detects signal within the depth up to 10 nm, the growth of SEI on the electrode surface decreases the signal of nitrogen in ADALS. Nevertheless, the atomic content of nitrogen increases from 3.6% in the pristine electrode to 3.9% in the fully discharged electrode and 5.7% in the fully charged electrode, indicating the existence of organic nitrogen matrix in the SEI. Hence, ADALS may participate in the formation of an SEI, contributing to the generation of organic nitrogen matrix. After ADALS is charged back to 3 V, the lithiated azo peak at 398.3 eV disappears (Fig. 4*F*), while there is only one strong peak at 400.2 eV, representing the azo group in ADALS and organic nitrogen matrix in the SEI. The impurity peaks disappear at the fully charged state, because of the SEI layer.

The redox reactions of azo compounds were further examined using DFT calculations as shown in Fig. 5 *A*–*D*. Reduction potentials of the representative model compounds AB, ADA, Li_2ADA, and Li_3ADA were predicted to be 1.26–1.45 V vs. Li/Li^+ with the transferred electron situated at the *N*-*N* fragment for the reduced species. Increasing the size of the model compound Li_2ADA to $(Li_2ADA)_4$ to make it more representative of the electrode slightly increased the reduction potential to 1.53 V vs. Li/Li^+, bringing it in excellent agreement with experimental values. The azo group redox reaction serves as a driving force for lithium intercalation/deintercalation that is further investigated using periodic DFT calculations shown in Fig. 5 *E*–*G*. Numerous possible crystal structures were investigated (see *SI Appendix*, Fig. S16 for the representative Li_4ADA structures); only the most stable crystal structures are shown in Fig. 5 *E*–*G*. DFT calculations predict intercalation potentials of Li_3ADA vs. Li_2ADA and Li_4ADA vs. Li_3ADA to be 1.58 V and 1.48 V vs. Li/Li^+, respectively. These predictions are in excellent agreement with the experimentally measured galvanostatic charge–discharge curves shown in Figs. 2*A* and 3*A*, further confirming the proposed mechanism of the Li binding to azo groups of ADALS. Electronic properties of AB and ADALS were also examined by visualizing the energy levels of the lowest unoccupied molecular orbital (LUMO) and the highest occupied molecular orbital (HOMO) for AB and ADALS as shown in *SI Appendix*, Fig. S17. The charge-density isosurfaces of LUMO states for AB and ADALS demonstrate that an electron will localize in the nitrogen of the azo group after lithiation, confirming the azo group is the electrochemical active site for the reduction of the azo compound. It is consistent with the reduction calculations shown in Fig. 5 *A*–*D*. The smaller energy gap between LUMO and HOMO levels in ADALS than that in AB suggests ADALS has higher intrinsic electronic conductivity than AB (14). We also calculate the possibility of the reaction between a carbonyl group and Li ion. As indicated by *SI Appendix*, Fig. S18*A*, the lithiated carboxylate groups in ADALS generated by the reaction between a carbonyl group and Li ion are unstable, and will be dissociated to Li_2O. To confirm our calculation results, we replace the azo group in ADALS with vinyl group (C=C) (*SI Appendix*, Fig. S18*B*), and the carbonyl groups show a reversible lithiation/delithiation potential of 0.77 V, in line with the reported potential of similar compounds in the literatures (37, 38). Therefore, the experimental and theoretical results confirm that the azo group acts as an electrochemical active site to react with Li ion in LIBs.

Since ADALS exhibited promising performance in LIBs, its performance in SIBs was also evaluated. As shown in Fig. 6*A*, the galvanostatic charge–discharge curves of ADALS in SIBs display a pair of charge/discharge plateaus at 1.2 V/1.4 V, which is 0.3 V lower than that in LIBs, and a reversible capacity of 153 mAh g^{-1} is delivered in the first cycle. The FCE of ADALS in SIBs is only 41.6%, which is much lower than that (77%) in LIBs. According to a previous report, there is an ion-exchange process during the cycling of sodium-salt electrode in LIBs, which lowers the Coulombic efficiency of the sodium-salt electrode in LIBs (10). In this work, ADALS is a lithium salt. When it is cycled in SIBs, a similar ion-exchange process occurs, resulting in a low Coulombic efficiency. To improve the Coulombic efficiency, azobenzene-4,4′-dicarboxylic acid sodium-salt (ADASS) was synthesized. When ADASS is cycled in SIBs, its FCE is increased to 75% (*SI Appendix*, Fig. S19), which is close to the FCE of ADALS in LIBs. Therefore, the poor Coulombic efficiency of ADALS in SIBs is due to the ion-exchange process between the lithium salt (ADALS) and sodium electrolyte. The Coulombic efficiency can be enhanced by using sodium salt (ADASS) in SIBs. In the long-term cycling test (Fig. 6*B*), a reversible capacity of 140 mAh g^{-1} at 1 C is retained after 500 cycles with a very slow capacity decay rate of 0.017% per cycle. Moreover, the Coulombic efficiency of ADALS in SIBs is close to 100%, indicating the superior cycling stability. Therefore, the excellent electrochemical performance of ADALS in LIBs and SIBs demonstrates that azo compounds are universal for alkali-ion batteries.

Conclusions

In summary, we reported a type of organic compounds for green and sustainable alkali-ion batteries. In these organic compounds, the azo group (N=N) functions as an active site for reversible lithiation/delithiation, representing a chemistry for organic alkali-ion batteries. The reaction mechanism of the azo compounds

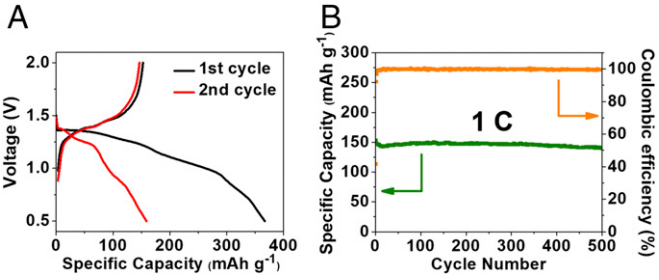

Fig. 6. The electrochemical performance of ADALS in Na-ion batteries. (*A*) The galvanostatic charge–discharge curves at 1 C. (*B*) Desodiation capacity and Coulombic efficiency versus cycle number at the current density of 1 C.

is investigated by XRD, Raman spectroscopy, XPS, and DFT calculations, demonstrating that one azo group can reversibly react with two Li ions through the interaction between N and Li. As a model azo compound, the ADALS-based electrode shows one of the best electrochemical performances in organic electrodes. It delivers reversible capacities of 179 mAh g^{-1} at 0.5 C for 100 cycles, 146 mAh g^{-1} at 2 C for 2,000 cycles, and 93 mAh g^{-1} at 20 C for 5,000 cycles, demonstrating the high cycling stability and fast charge/discharge capability. Superior electrochemical performance is also achieved in SIBs, indicating that azo compounds are universal electrode materials for alkali-ion batteries.

Methods

Material Synthesis. AB, MRSS, and 4-nitrobenzoic acid were purchased from Sigma-Aldrich and used as received. Azobenzene-4,4′-dicarboxylic acid was prepared based on the synthetic route in literature (39). ADALS were prepared as follows: Azobenzene-4,4′-dicarboxylic acid was dispersed in ethanol alcohol with lithium hydroxide powders in 5% excess. The solution was stirred at room temperature for 24 h, and then the solution was filtered to collect the precipitation. The precipitations (ADALS) were washed with ethanol and dried in the vacuum oven at 100 °C overnight. All of the materials were analyzed by mass spectrometry in *SI Appendix*, Fig. S20.

Material Characterizations. The XRD pattern was recorded by a Bruker Smart1000 (Bruker AXS Inc.) using CuKα radiation; Raman measurements were performed on a Horiba Jobin Yvon Labram Aramis using a 532-nm diode-pumped solid-state laser, attenuated to give ∼900-μW power at the sample surface; FTIR was recorded by NEXUS 670 FT-IR Instrument; Mass spectrometry: The anions of the salts were characterized with electrospray ionization time-of-flight mass spectrometry (AccuTOF; JEOL). Mass spectra were acquired under negative mode with the following parameters: capillary voltage, 2,100 V; orifice 1 voltage, 20 V; orifice 2 voltage, 5 V; ring voltage, 5 V; dissolution temperature 100 °C. SEM images were taken by Hitachi SU-70 analytical ultrahigh-resolution SEM (Japan); XPS data were collected on a Kratos Axis 165 X-ray photoelectron spectrometer operating in hybrid mode using monochromatic Al Kα (1,486.7 eV) X-rays. High-resolution data were collected at a pass energy of 40 eV, and charge neutralization was required to minimize sample charging. XPS data were analyzed using CASA XPS software, using peaks with a 70% Gaussian/30% Lorentzian peak shape after subtraction of a Shirley background.

Electrochemical Measurements. The organic compounds were mixed with carbon black and sodium alginate binder to form a slurry at the weight ratio of 60:30:10 [polyvinylidene fluoride (PVDF) binder is used for an electrode based on AB due to its strong hydrophobic property]. The electrode was prepared by casting the slurry onto aluminum foil using a doctor blade and dried in a vacuum oven at 100 °C overnight (an electrode based on AB was dried at 60 °C overnight due to its low melting and boiling point). The slurry coated on aluminum foil was punched into circular electrodes with an area mass loading of ∼1.5 mg cm^{-2}. Coin cells for LIBs were assembled with lithium metal as the counter electrode, 6 M LiTFSI in a mixture of DOL/DME (1:1 by volume) or 1 M $LiPF_6$ in EC/DEC (1:1 by volume) electrolyte and Celgard3501 (Celgard, LLC Corp.) as the separator. Coin cells for sodium-ion batteries were assembled with sodium metal as the counter electrode, 1 M $NaPF_6$ in diethylene glycol dimethyl ether electrolyte and Celgard3501 (Celgard, LLC Corp.) as the separator. Electrochemical performance was tested using an Arbin battery test station (BT2000; Arbin Instruments). Cyclic voltammograms were recorded using a Gamry Reference 3000 Potentiostat/Galvanostat/ZRA with a scan rate of 0.1 mV s^{-1}. Impedance analysis was also performed by a Gamry Reference 3000 Potentiostat/Galvanostat/ZRA.

ACKNOWLEDGMENTS. We acknowledge the support of the Maryland NanoCenter and its NispLab. The NispLab is supported in part by the NSF as a Materials Research Science and Engineering Center (MRSEC) Shared Experimental Facility. This work was supported by the US National Science Foundation Award 1438198.

1. Larcher D, Tarascon JM (2015) Towards greener and more sustainable batteries for electrical energy storage. *Nat Chem* 7:19–29.
2. Grey CP, Tarascon JM (2016) Sustainability and in situ monitoring in battery development. *Nat Mater* 16:45–56.
3. Zhao Q, Lu Y, Chen J (2017) Advanced organic electrode materials for rechargeable sodium-ion batteries. *Adv Energy Mater* 7:1601792.
4. Schon TB, McAllister BT, Li PF, Seferos DS (2016) The rise of organic electrode materials for energy storage. *Chem Soc Rev* 45:6345–6404.
5. Liang Y, et al. (2017) Universal quinone electrodes for long cycle life aqueous rechargeable batteries. *Nat Mater* 16:841–848.
6. Liang Y, Tao Z, Chen J (2012) Organic electrode materials for rechargeable lithium batteries. *Adv Energy Mater* 2:742–769.
7. Muench S, et al. (2016) Polymer-based organic batteries. *Chem Rev* 116:9438–9484.
8. Morita Y, et al. (2011) Organic tailored batteries materials using stable open-shell molecules with degenerate frontier orbitals. *Nat Mater* 10:947–951.
9. Wu YL, et al. (2017) G-quadruplex organic frameworks. *Nat Chem* 9:466–472.
10. Luo C, et al. (2014) Self-assembled organic nanowires for high power density lithium ion batteries. *Nano Lett* 14:1596–1602.
11. Chen H, et al. (2009) Lithium salt of tetrahydroxybenzoquinone: Toward the development of a sustainable Li-ion battery. *J Am Chem Soc* 131:8984–8988.
12. Lee M, et al. (2013) Redox cofactor from biological energy transduction as molecularly tunable energy-storage compound. *Angew Chem Int Ed Engl* 52:8322–8328.
13. Hong J, et al. (2014) Biologically inspired pteridine redox centres for rechargeable batteries. *Nat Commun* 5:5335.
14. Peng C, et al. (2017) Reversible multi-electron redox chemistry of π-conjugated N-containing heteroaromatic molecule-based organic cathodes. *Nat Energy* 2:17074.
15. Liang Y, Zhang P, Chen J (2013) Function-oriented design of conjugated carbonyl compound electrodes for high energy lithium batteries. *Chem Sci* 4:1330–1337.
16. Chen H, et al. (2008) From biomass to a renewable $Li_xC_6O_6$ organic electrode for sustainable Li-ion batteries. *ChemSusChem* 1:348–355.
17. Armand M, et al. (2009) Conjugated dicarboxylate anodes for Li-ion batteries. *Nat Mater* 8:120–125.
18. Wang S, et al. (2013) Organic $Li_4C_8H_2O_6$ nanosheets for lithium-ion batteries. *Nano Lett* 13:4404–4409.
19. Liang Y, Zhang P, Yang S, Tao Z, Chen J (2013) Fused heteroaromatic organic compounds for high-power electrodes of rechargeable lithium batteries. *Adv Energy Mater* 3:600–605.
20. Song Z, et al. (2015) Polyanthraquinone as a reliable organic electrode for stable and fast lithium storage. *Angew Chem Int Ed Engl* 54:13947–13951.
21. Song Z, Zhan H, Zhou Y (2010) Polyimides: Promising energy-storage materials. *Angew Chem Int Ed Engl* 49:8444–8448.
22. Nokami T, et al. (2012) Polymer-bound pyrene-4,5,9,10-tetraone for fast-charge and -discharge lithium-ion batteries with high capacity. *J Am Chem Soc* 134:19694–19700.
23. Häupler B, Wild A, Schubert US (2015) Carbonyls: Powerful organic materials for secondary batteries. *Adv Energy Mater* 5:1402034.
24. Guo J, Yang Z, Yu Y, Abruña HD, Archer LA (2013) Lithium-sulfur battery cathode enabled by lithium-nitrile interaction. *J Am Chem Soc* 135:763–767.
25. Tecklenburg MMJ, Kosnak DJ, Bhatnagar A, Mohanty DK (1997) Vibrational characterization of azobenzenes, azoxybenzenes and azoaromatic and azoxyaromatic polyethers. *J Raman Spectrosc* 28:755–763.
26. Mohammed IA, Mustapha A (2010) Synthesis of new azo compounds based on N-(4-hydroxypheneyl)maleimide and N-(4-methylpheneyl)maleimide. *Molecules* 15:7498–7509.
27. Augustyn V, et al. (2013) High-rate electrochemical energy storage through Li^+ intercalation pseudocapacitance. *Nat Mater* 12:518–522.
28. Wang C, et al. (2015) Extended π-conjugated system for fast-charge and -discharge sodium-ion batteries. *J Am Chem Soc* 137:3124–3130.
29. Xu K (2014) Electrolytes and interphases in Li-ion batteries and beyond. *Chem Rev* 114:11503–11618.
30. Kasavajjula U, Wang C, Appleby AJ (2007) Nano- and bulk-silicon-based insertion anodes for lithium-ion secondary cells. *J Power Sources* 163:1003–1039.
31. Zhang W (2011) A review of the electrochemical performance of alloy anodes for lithium-ion batteries. *J Power Sources* 196:13–24.
32. Xu Y, et al. (2016) New nitrogen-rich azo-bridged porphyrin conjugated microporous networks for high performance of gas capture and storage. *RSC Adv* 49:30048–30055.
33. Russat J (1988) Characterization of polyamic acid/polyimide films in the nanometric thickness range from spin-deposited polyamic acid. *Surf Interface Anal* 11:414–420.
34. Kokai F, Saito H, Fujioka T (1989) X-ray photoelectron spectroscopy studies on modified polyimide surfaces after ablation with a KrF excimer laser. *J Appl Phys* 66:3252–3255.
35. Yue J, Epstein AJ (1991) XPS study of self-doped conducting polyaniline and parent systems. *Macromolecules* 24:4441–4445.
36. Mohtasebi A, Chowdhury T, Hsu LHH, Biesinger MC (2016) Interfacial charge transfer between phenyl-capped aniline tetramer films and iron oxide surfaces. *J Phys Chem C* 120:29248–29263.
37. Walker W, Grugeon S, Armand M, Tarascon J (2011) Electrochemical characterization of lithium 4,4′-tolane-dicarboxylate for use as a negative electrode in Li-ion batteries. *J Mater Chem* 21:1615–1620.
38. Fédèle L, et al. (2017) 2D-layered lithium carboxylate based on biphenyl core as negative electrode for organic lithium-ion batteries. *Chem Mater* 29:546–554.
39. Kenawy ER, Aly ES, Imam Abdel-Hay F, Abdeen R, Mahmoud YAG (2011) Synthesis and microbial degradation of azopolymers for possible applications for colon specific drug delivery I. *J Saudi Chem Soc* 15:327–335.